Nanoscale

ROYAL SOCIETY OF CHEMISTRY

PAPER

View Article Online
View Journal | View Issue

Cite this: *Nanoscale*, 2024, **16**, 15265

Transparent TiO_2 nanotubes supporting silver sulfide for photoelectrochemical water splitting†

Wiktoria Lipińska,[a] Stefania Wolff,[a,b] Katharina E. Dehm,[c] Simon P. Hager,[c] Justyna Gumieniak,[d] Agnieszka Kramek,[d] Ryan W. Crisp,[c] Emerson Coy,[e] Katarzyna Grochowska[a] and Katarzyna Siuzdak *[a]

Received 2nd April 2024,
Accepted 16th July 2024

DOI: 10.1039/d4nr01440e

rsc.li/nanoscale

Differences between photoelectrochemical and electrochemical activity were thoroughly investigated for the oxygen evolution reaction mediated by Ag_2S deposited on two types of ordered titania substrates. Titanium dioxide nanotubes were fabricated by anodization of magnetron sputtered Ti films on ITO-coated glass substrates or directly from Ti foil. Further, Ag_2S deposition on the nanotubes was carried out using successive ionic layer adsorption and reaction, known as SILAR, with 5, 25, and 45 cycles performed. Two types of nanotubes, one on transparent the other on non-transparent substrates were compared regarding their geometry, structure, optical, and electrochemical properties. It was demonstrated that the composite of Ag_2S grown on transparent nanotubes exhibits higher catalytic activity compared to Ag_2S grown on the nanotubes formed on Ti foil. The results showed that transparent nanotubes after modification with Ag_2S by 25 SILAR cycles exhibit *ca.* 3 times higher photocurrent under visible light illumination than non-transparent ones treated with the same number of cycles. Furthermore, transparent nanotubes after 45 SILAR cycles of Ag_2S exhibit enhanced activity towards oxygen evolution reaction with 9.3 mA cm^{-2} at 1.1 V *vs.* Ag/AgCl/0.1 M KCl which is six times higher than titania alone on Ti foil.

1. Introduction

In the world of increasing global energy demand, sustainable and renewable energy sources have become indispensable. As fossil fuel resources dwindle and environmental concerns intensify, scientists are developing innovative solutions to meet the growing energy needs of society. The combustion of carbon-based materials releases greenhouse gases which contribute significantly to negative climate changes and degradation of the environment. Therefore, renewable energy sources such as solar, wind, hydropower, biomass, or geothermal offer attractive alternatives without depleting limited resources.[1] Among others, the water splitting process to produce hydrogen used in fuel cell technology is a promising route forward. The water electrolysis process utilizes electrodes coated with a catalyst to perform the reaction. Conventional catalysis is done with noble metals or metal oxides, however, metal sulfides are increasingly being explored as a lower cost alternative.[2] Metal sulfides are a class of compounds in which a sulfur (S) anion is combined with a metal (M) cation labelled as M_xS_y forming sulfides of various stoichiometry.[3] Up to now, various metal sulfides like CdS,[4] Ag_2S,[5] PbS,[6] NiS_y,[7] CoS_y,[8] and FeS_y [9] have been implemented for oxygen and hydrogen evolution reactions. Typically, sulfur is in the −2 oxidation state and the metal in the +2, +3, or +4 oxidation state. Their unique optical, electrical, and catalytical properties such as bandgap tunability,[10] low valence band level,[11] quantum size effect,[12] facile synthesis methodology,[13] and exposed catalytic sites[3] position them as promising candidates for energy conversion applications. Among others, silver sulfide extends its applicability in many fields especially in photodetectors,[14] solar cells,[15] and catalysts for example in the oxygen reduction reaction[16] or oxygen evolution reaction (OER).[17] Ag_2S is an n-type semiconductor with a narrow band gap of 1 eV.[18] Furthermore, it exhibits strong absorption from the ultraviolet through the visible spectrum and near-infrared regions.[14] Investigation of the catalytic activity of Ag_2S towards OER shows that the

---

[a] *Centre for Plasma and Laser Engineering, Institute of Fluid-Flow Machinery, Polish Academy of Sciences, Fiszera 14 Street, 80-231 Gdańsk, Poland. E-mail: ksiuzdak@imp.gda.pl*

[b] *Faculty of Applied Physics and Mathematics, Institute of Nanotechnology and Materials Engineering, Gdańsk University of Technology, Narutowicza 11/12 Street, 80-233 Gdańsk, Poland*

[c] *Chemistry of Thin Film Materials, Department of Chemistry and Pharmacy, Friedrich-Alexander-Universität Erlangen-Nürnberg, Cauerstrasse 3, 91058 Erlangen, Germany*

[d] *The Faculty of Mechanics and Technology, Rzeszów University of Technology, Kwiatkowskiego 4 Street, 37-450 Stalowa Wola, Poland*

[e] *NanoBioMedical Centre, Adam Mickiewicz University, Wszechnicy Piastowskiej 3 St, 61-614 Poznań, Poland*

† Electronic supplementary information (ESI) available. See DOI: **https://doi.org/10.1039/d4nr01440e**

common practice is to combine silver with another metal to increase the catalytic activity. However, this work aims to explore Ag_2S alone without transition metal co-catalysts like Ni,[17] Co,[17] or Fe[19] usually used for oxygen evolution processes.

Here, we present the fabrication process where both transparent and non-transparent TiO_2 nanotube substrates were modified by successive ionic layer adsorption and reaction (SILAR) of Ag_2S and thermal treatment. Titanium dioxide nanotubes were chosen as a platform for metal sulfide modification because of their high degree of ordering, larger surface area than planar films, and strong absorption of UV light which can be tuned by the addition of other photosensitizers, thereby leading to an enhancement of charge collection with visible light illumination.[20,21] The electrochemical and photoelectrochemical properties of Ag_2S on transparent TiO_2 nanotubes fabricated on ITO-coated glass were compared with non-transparent nanotubes fabricated on Ti foil, indicating significant changes in the properties of the electrode material depending on the chosen titania support. The electrochemical measurements were carried out in two different electrolytes: 0.5 M Na_2SO_4 and 0.5 M NaOH, with which the material's (photo)activity toward OER was investigated.

2. Experimental

2.1. Reagents

ITO glass substrates (S111, thickness: 1.1 mm, ITO thickness: 100 nm, Ossila), titanium foil (99.7%, thickness: 0.127 mm, Strem), acetone (99.5%, Chempur), ethanol (96%, Chempur), 2-propanol (99.7%, Chempur), ethylene glycol (99.5% Chempur), phosphoric acid (85%, Chempur), ammonium fluoride (98%, Chempur), silver nitrate (POCH), sodium sulfide nonahydrate (98%, Sigma-Aldrich).

2.2. Electrode fabrication

The ITO substrates with a size of 1.5 × 2 cm^2 were ultrasonically cleaned in water, ethanol, acetone, and isopropanol for 15 min. The thin Ti interlayer was deposited for 15 seconds using magnetron sputtering at a current of 0.412 A, argon flow of 1 sccm, and pressure of 2.0×10^{-3} Pa (nanoPVD, Moorfield). This initial Ti layer was thermally treated for 3 min at 400 °C on a hot plate (PCE-E6000 Serials). Then, a second round of magnetron sputtering for 30 min was performed to obtain the main Ti layer with a current 0.412 A, argon flow of 2 sccm, and a pressure of 2.0×10^{-3} Pa leading to a film thickness of *ca.* 400 nm, verified by profilometry (DektakXT, Bruker). Titania nanotubes were fabricated using an anodization process in a two-electrode system, where the Ti on ITO was the anode and a Pt mesh was the cathode. The Ti electrodes were placed in a custom holder where only a defined part of the sample was anodized, namely a circle-shaped area with a diameter of 10 mm (see Fig. 1c). The electrolyte contained 0.27 M NH_4F/1 M H_3PO_4/1 vol% H_2O/99 vol% ethylene glycol. The anodization was carried out at a temperature of 23 °C controlled with a thermostat and an applied voltage of 40 V for 60 min. Next, the electrodes were thermally treated at 450 °C for 1 h in a tube furnace in ambient atmosphere. Herein, these electrodes are designated as gTiNT. The first letter "g" indicates a glass substrate was used as a support for the titanium deposition. Alternatively, titania nanotubes were fabricated on Ti foil. First, Ti foil was cut into 2 × 3 cm^2 plates and ultrasonically cleaned in acetone, ethanol, and water for 10 min. The electrolyte contained 0.27 M NH_4F/15 vol% H_2O/85 vol% ethylene glycol. The anodization was performed under temperature of 23 °C and voltage 40 V for 1 h. After anodization the samples were annealed in a tube furnace for 1 h at a temperature of 450 °C also in air. These samples are designated fTiNT. The first letter "f" indicating the material was fabricated on foil. Finally, SILAR was carried out both on gTiNT and fTiNT sample sets using silver and sulfur ionic solutions with different numbers of deposition cycles. Before the first SILAR cycle, the electrodes were placed in UV light and ozone for 30 min. Then the modification consisting of 5, 25, and 45 SILAR cycles was performed. The samples were immersed in aqueous 5 mM $AgNO_3$ for 30 min and then in 5 mM Na_2S for 30 min. The samples were rinsed then with DI water and dried. The procedure was further repeated for the given cycle numbers with the time of the subsequent solution immersion decreased to 2 min. The last step was to anneal in argon for 1 h at the temperature of 250 °C.

2.3. Sample characterisation

The morphology of the electrodes was analysed by scanning electron microscopy (SEM) and energy dispersive X-ray spectroscopy (EDX) acquired with a JEOL JSM-F100. Furthermore, Grazing Incidence X-ray Diffraction (Gi-XRD) was used to study the crystallographic structure. Samples were measured in a Panalytical Empyrean, equipped with a Cu lamp working at 4–5 kV 40 mA. The *z* position of the samples was optimised to faintly detect the most intensive peak of the samples (~25°) and increments of omega (incident angle) between 0.01 and 10° (Ω) were used to collect spectra from 15 to 50° of 2θ. Samples are represented in a contour map in log scales in *y* and *z*. Penetration depth was calculated according to the density of the TiO_2 and the Cu K-alpha (1.5406 Å) wavelength. The optical properties of the electrodes were inspected using an UV-vis spectrophotometer (Lambda 35 PerkinElmer). The spectra were recorded in the wavelength range from 300 to 900 nm.

The chemical structure of the samples was measured by X-ray photoelectron spectroscopy using a Thermo Scientific™ K-Alpha™ X-ray photoelectron spectrometer (XPS). The samples were irradiated with Al Kα = 1486.7 eV X-ray radiation. Measurements were carried out under a pressure of 10^{-9} to 10^{-8} mbar. Survey spectra were registered using a pass energy of 150 eV and a step size of 1 eV. The equipment was calibrated using C 1s (284.5 eV). High-resolution spectra were recorded for the oxygen O 1s, titanium Ti 2p, carbon C 1s, silver Ag 3d, and sulfur S 2p binding energy regions using a pass energy of 20 eV and step size of 0.1 eV.

Raman spectra were recorded by means of a confocal micro-Raman spectrometer (InVia, Renishaw) with sample excitation by an argon ion laser emitting at 514 nm and operating at 10% of its total power from 100 to 1500 cm^{-1}. The

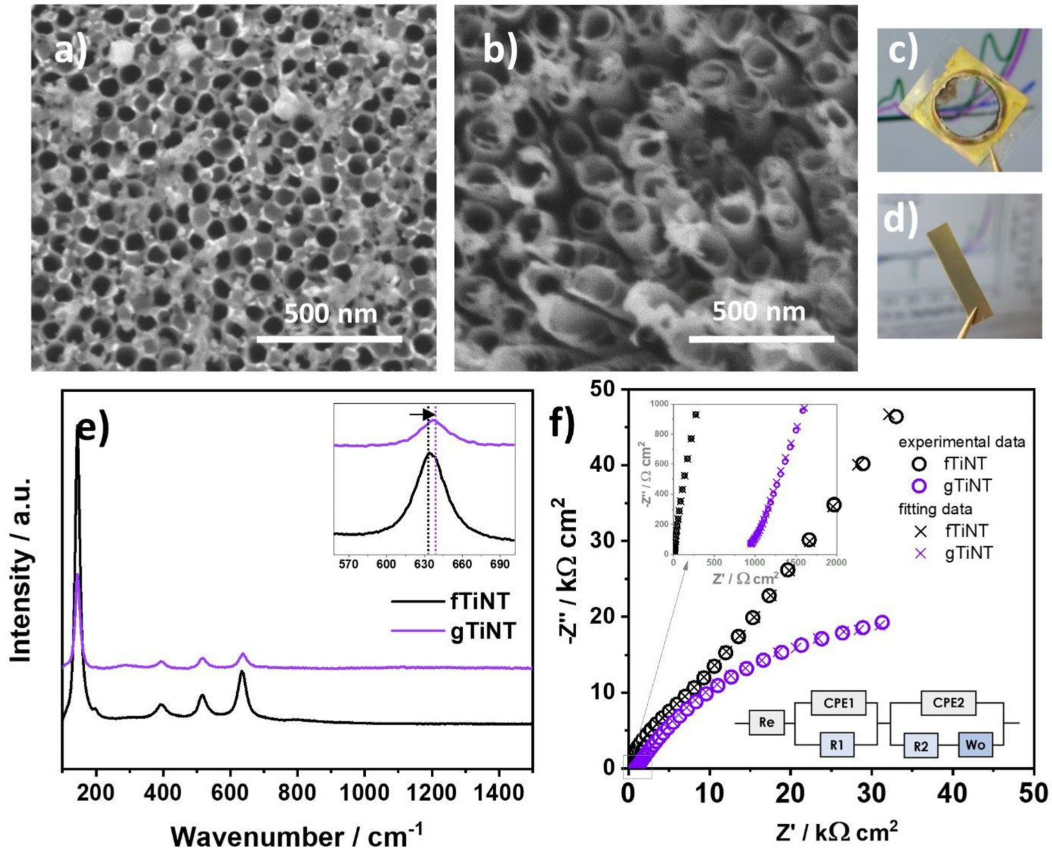

Fig. 1 SEM images of (a) gTiNT, (b) fTiNT, electrode photography of (c) gTiNT, (d) fTiNT, (e) Raman spectra for gTiNT and fTiNT, (f) Nyquist representation of impedance spectra recorded for gTiNT and fTiNT at OCP.

Raman spectra were inspected for gTiNT and fTiNT samples as well as for 5-Ag_2S/gTiNT, 25-Ag_2S/gTiNT, 45-Ag_2S/gTiNT electrodes before electrochemical measurements and after 3 and 10 CVs cycles in 0.5 M Na_2SO_4 and 0.5 M NaOH solutions.

Electrochemical and photoelectrochemical measurements were carried out in a 3-electrode system, where the TiO_2-based electrodes were used as the working electrode, Pt mesh as a counter electrode, and Ag/AgCl/0.1 M KCl as a reference electrode. The electrolyte was deaerated with argon, and, during the measurements, argon flow was kept above the electrolyte. The photoelectrochemical measurements were carried out using an AutoLab PGStat 302N potentiostat-galvanostat. Cyclic voltammetry (CV) and linear voltammetry (LV) scans were recorded in 0.5 M Na_2SO_4 solution in the range from −1 V to +1 V *vs.* Ag/AgCl/0.1 M KCl. The CVs were performed with a scan rate of 50 mV s^{-1}, while the LVs with a scan rate of 10 mV s^{-1}. The LV curves were recorded under chopped visible light illumination provided by a xenon lamp (LOT-Quantum Design GmbH) with a cut off filter for wavelengths below 420 nm. The light intensity was calibrated by a silicon reference cell (Rera) to provide 100 mW cm^{-2}. The electrochemical measurements were carried out using an AutoLab 204 potentiostat-galvanostat. The CVs measurements were taken in deaerated 0.5 M NaOH solution in the range from −0.4 V to +1.1 V *vs.* Ag/AgCl/0.1 M KCl (see Fig. 7 and 8). The CVs were performed with a scan rate of 50 mV s^{-1}. The stability tests were carried out using both CA and CV techniques. In the case of chronoamperommetry, the current was recorded at +1.0 V (and for comparison at +0.5 V) *vs.* Ag/AgCl/0.1 M KCl lasted 10 000 s that is *ca.* 3 hours. Regarding CV, the multicyclic studies (100 cycles) were carried out for 45-Ag2S/gTiNT and the potential was changed from −0.4 to +1.1 V *vs.* Ag/AgCl/0.1 M KCl. Both results are shown in ESI file as Fig. S7.† The impedance spectra were recorded at OCP that equals +0.1 V *vs.* Ag/AgCl/0.1 M KCl, in the range from 10 Hz to 0.1 Hz with 10 mV amplitude of AC signal. The fitting procedure was carried out with EIS Analyser program[22] and using the proposed electric equivalent circuit (EQC) that will be discussed later on. The modified Powell algorithm was used with amplitude weighting r_a:

$$r_a(\omega, P_1, \ldots P_M) = {r_c}^2/(N-M) \tag{1}$$

where N is the number of points, M is the number of parameters, ω is the angular frequency, $P_1 \ldots P_M$ are parameters. Parameter r_c is defined as:

$${r_c}^2 = \sum_{i=1}^{N} \frac{(Z'_i - Z'_{i_{\text{calc}}})^2 + (Z''_i - Z''_{i_{\text{calc}}})^2}{Z'^2_i + Z'^2_{i_{\text{calc}}}} \tag{2}$$

where i corresponds to the measured values of impedance and $i_{\text{calc.}}$ is attributed to the calculated values; N is the number of points.

3. Results

3.1 Characterisation of transparent and non-transparent titania nanotubes

3.1.1. Differences between TiO_2 nanotubes fabricated on ITO and Ti foil. Titanium dioxide nanotubes exhibit varied morphological, structural, and electrochemical properties. Morphological alterations impact their surface area and therefore their photocatalytic efficiency. Here, electrochemical anodization processing results in formation of aligned nanotubes (see Fig. 1a and b). The outer diameter of TiO_2 nanotubes fabricated on ITO substrates is equal to 46 ± 10 nm, whereas, in the case of TiO_2 nanotubes fabricated on Ti foil the diameter reaches 124 ± 10 nm. In both cases, the electrochemical anodization process was carried out at a temperature of 23 °C, applied voltage of 40 V, duration of 1 h, and in a hydrated ammonium fluoride in ethylene glycol electrolyte. It should be noted that anodization of TiO_2 nanotubes on various substrates like ITO and Ti foil yields diverse morphologies and growth mechanisms. Ti/ITO substrates promote faster growth compared to Ti foil which can be attributed to a thinner Ti layer. According to Sivaprakash *et al.*,[23] high water content leads to an increased oxide dissolution rate and ion mobility. In our previous work[24] and this work, 15 vol% H_2O is used for anodization of the Ti foil to obtain aligned TiO_2 nanotubes. In the case of Ti on ITO, it can be too high of a concentration which leads to etching of the Ti and ITO surface. Therefore, the electrolyte for the gTiNT contained only 1 vol% H_2O. As can be seen in Fig. 1c, a transparent circle-shaped area is where nanotubes are present. According to Hankova *et al.*,[25] the anodization process of Ti sputtered on ITO carried out in 5 vol% H_2O in ethylene-based electrolyte results in the formation of transparent TiO_2 nanotubes. With the usage of 1 vol% H_2O it was possible to obtain completely non-transparent nanostructures (Fig. 1d). The Raman spectra of the fTiNT and gTiNT are shown in Fig. 1e. Raman bands associated with the anatase phase of TiO_2 [26] are located at 145, 198, 394, 516, and 634 cm^{-1}. The slight blue shift from 634 to 637 cm^{-1} between the fTiNT and the gTiNT electrode can be correlated with lack of impurities.[27] It should be mentioned that with the foil having 99.7% purity whereas the sputter target used for Ti deposition has a purity of 99.99%, a consequence is that the obtained nanotubes can have a slightly different content of impurities. Electrochemical impedance spectroscopy was used to determine the charge transfer resistance of the fTiNT and gTiNT electrodes (Fig. 1f). The impedance spectra were recorded in 0.5 M Na_2SO_4 solution at open circuit potential (OCP). The Re(CPE1R1)(CPE2R2Wo) equivalent circuit was proposed that is frequently used in works focused on the electrochemical studies of the titania nanotubes.[28,29] The electrolyte resistance is assigned to Re, while the subsequent EQC parts: (CPE1R1) and (CPE2R2Wo) are introduced to represent two time constants related to the inner and outer porous layer of titania. CPE instead of pure capacitance is used due to the electrode porosity represented by titanium dioxide nanotubes. The impedance of CPE is defined as $Z = Q^{-1}(i\omega)^{-n}$, where energy dispersion denoted as n is considered. The value of n is between 0.54–0.86 which results from the high porosity and is the consequence of the distribution of the relaxation times. W_o stands for Warburg open element and is assigned to the finite length diffusion with reflective boundary and described by:

$$Z_{W_o}(\omega) = \frac{\omega_{or}}{\sqrt{\omega}}(1-j)\coth[W_{oc}\sqrt{j\omega}] \tag{3}$$

where W_{or} stays for Warburg coefficient, $W_{oc} = d/D^{0.5}$. In the case of the studied material, W_o is related to the charge transport within tubular titania down to the blocking metal oxide support. The quality of fitting was on the level of 10^{-4} which suggests a good fit. The calculated values for each element in EQC for nanotubes formed onto Ti foil and ITO/glass substrate are collected in Table S1.† As can be seen, the most significant difference can be observed for resistance elements $R1$ and $R2$. In the case of $R1$, attributed to the outer porous layer, has the smallest value ($R1$ = 41 Ω cm^2) for gTiNT. On the other hand, the value of $R2$, which represents the resistance of the inner layer, is much lower for fTiNT ($R2$ = 7.1 Ω cm^2). Those differences are related to tubular geometry. According to SEM inspection, the outer diameter of gTiNT is almost 2.7 times lower than fTiNT. Thus, much more nanotubes are present on the same geometric area of glass substrate than on Ti foil and in consequence, the real surface area is much higher for gTiNT. A higher developed area gives higher space charge capacitance $Q1$ and lower resistance $R1$ that was obtained for gTiNT. The significantly higher value of resistance $R2$ for gTiNT, can result from the presence of some amorphous material, as was shown on Gi-XRD, at the barrier layer present between support and titania nanotubes. Regarding values of $Q2$, the higher one was found for gTiNT also results from the oxide film present at the bottom of nanotubes that could be more thick and porous than in the case of fTiNT.[30]

The fTiNT and gTiNT electrodes were examined using Gi-XRD (see Fig. 2). This technique confirmed the presence of anatase on both the surface and within the material. The results indicate a minor presence of amorphous titania (indicated in Fig. 2b) below the titanium nanotube surfaces, which is observed only in the ITO substrates and not on the metal foil. Gi-XRD results for all of the samples described in the manuscript are presented in Fig. S2.†

3.2. TiO_2 nanotubes modified by Ag_2S

3.2.1 Morphology. SEM images of Ag_2S-coated TiO_2 nanotubes fabricated on glass substrates are presented in Fig. 3a–f. The outer diameter of NTs for gTiNT, 5-Ag_2S/gTiNT, 25-Ag_2S/gTiNT, and 45-Ag_2S/gTiNT is equal to 46, 41, 42, and 42 ± 10 nm, respectively. For electrodes with Ag_2S deposition, the outer diameter become slightly smaller than for pure TiNTs. However, it should be noted that with an increase of SILAR cycles, the regular interior area of the nanotubes starts to disappear. This behaviour is mostly visible in the case of 45-Ag_2S/gTiNT electrode (see Fig. 3f). The number of cycles SILAR is reflected in the colour changes of the electrode surface. Initially pure gTiNT are completely transparent and with an

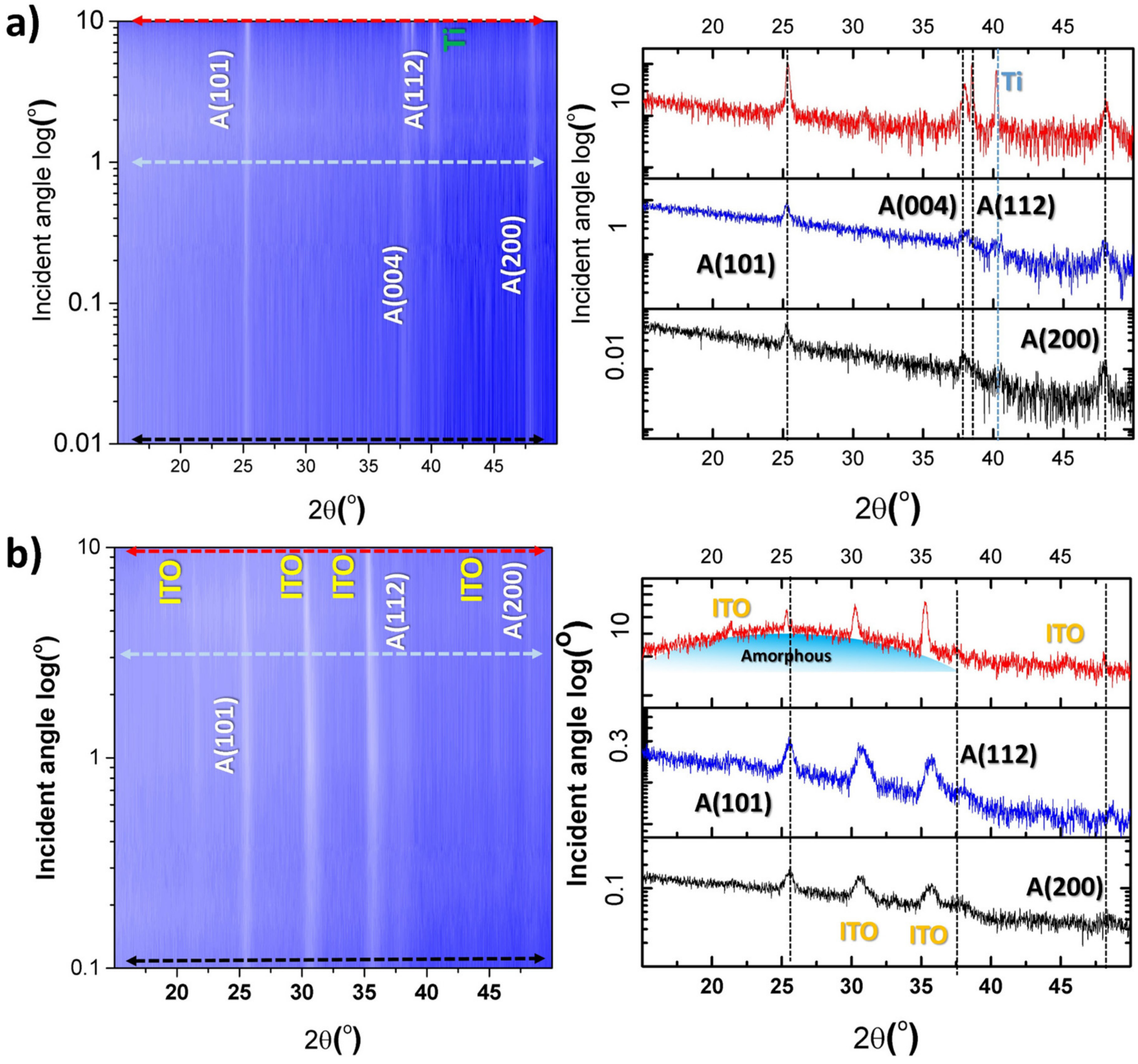

Fig. 2 Gi-XRD for (a) fTiNT and (b) gTiNT. Dashed lines show selected spectra at a given incident angle.

increase of Ag_2S modification cycles the electrodes become brown colored. SEM images of 5-Ag_2S/fTiNT, 25-Ag_2S/fTiNT, 45-Ag_2S/fTiNT are presented in Fig. S1 in ESI.†

Using EDX analysis, it was confirmed that Ag_2S is deposited (see Fig. S3 and Table S2†), however due to spectral overlaps and the large interaction volume, the assignment of exact atomic percentages and distributions throughout the tubes is obscured.

3.2.2. **Optical properties.** Fig. 4a and b shows absorbance and reflectance spectra for silver sulfide coated titania nanotubes grown on ITO or Ti foil, respectively. The reflectance spectrum was recorded for fTiNT materials due to the opaque substrate. Both pure TiO_2 NTs samples, namely gTiNT and fTiNT, exhibit absorption in the UV region, *i.e.* below 400 nm, with Raman spectral analysis indicating anatase as the main crystalline phase. However, for gTiNT one can observe fringes that appear from *ca.* 400 nm. This phenomenon can be explained by photonic nature of the material, *i.e.* constructive and destructive interference of reflected light due to the nanostructured titania nanotubes and bilayer structure of the TiNTs on ITO glass making the subtraction of reflectance not feasible.[24,31] Nonetheless, morphological features such as nanotube ordering as well as grain size may also affect the optical properties[32] as the optical response depends also on the nanotubes' geometry[33] which may explain the reason behind lack of the fringes for fTiNT.[34] Deposition of silver sulfide results in disappearance of the fringes for gTiNT and the increase of absorption in the visible range for both gTiNT and fTiNT substrates. This enhanced absorption is attributed to the narrow band gap (1.0 eV) and high absorption coefficient of Ag_2S.[35]

As can be seen for fTiNT and gTiNT electrodes, light is absorbed at longer wavelengths (lower energy) than the TiO_2 bandgap after coating the NTs with Ag_2S, as expected for a material of smaller bandgap. In order to determine the bangap value, we taken into account the values of the expo-

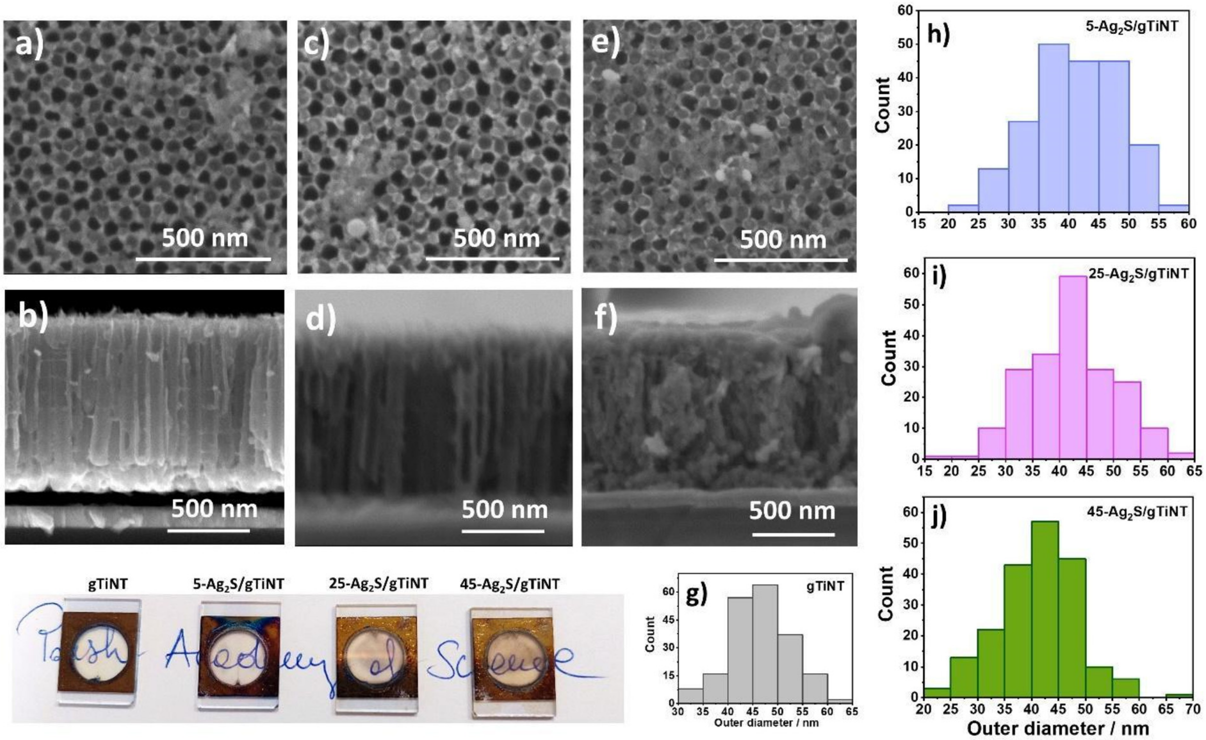

Fig. 3 SEM images of (a and b) 5-Ag_2S/gTiNT, (c and d) 25-Ag_2S/gTiNT, (e and f) 45-Ag_2S/gTiNT, and size distribution of TiO_2 nanotubes outer diameter (g) gTiNT, (h) 5-Ag_2S/gTiNT, (i) 25-Ag_2S/gTiNT, (j) 45-Ag_2S/gTiNT.

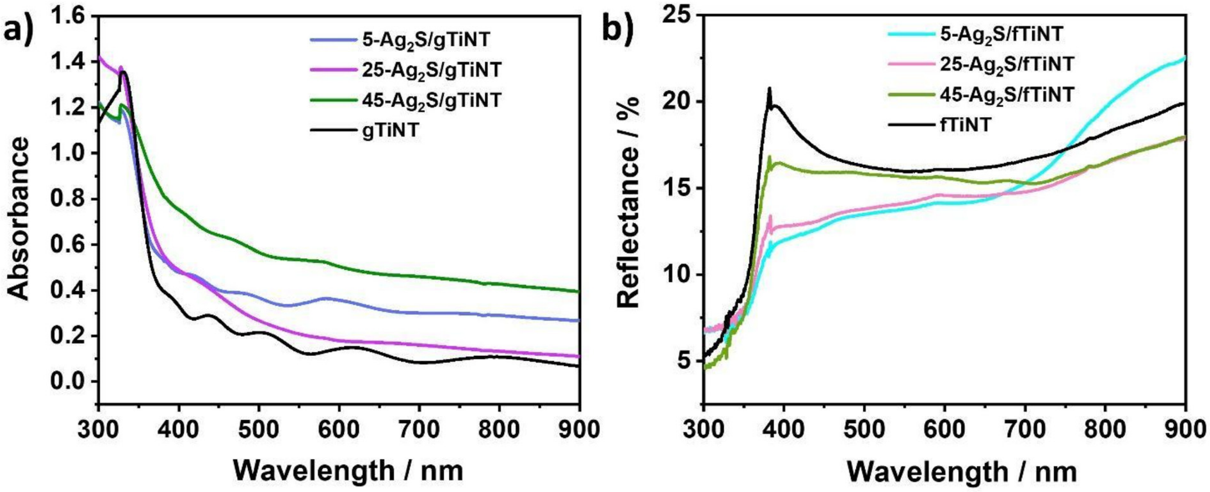

Fig. 4 UV-vis (a) absorbance spectra for Ag_2S-coated and non-coated gTiNT and (b) reflectance spectra for Ag_2S-coated and non-coated fTiNT.

nent in Tauc method typical for titania since amount of the TiO_2 nanotubes is much higher comparing to the decorating agent – silver sulphide. As can be seen, the values for fTiNT and gTiNT electrodes hardly differ (2.95 and 2.96 eV, respectively) and are narrower than the one reported for bulk anatase −3.2 eV. However, it should be taken into account that the energy bandgap of the nanomaterial depends on its geometry.[36] For both types of substrates, the values of energy bandgap are lower than for pure titania nanotubes which was expected as the NTs were covered with the material of smaller energy bandgap. For modified gTiNT, the energy bandgap values decrease with increased cycles which is in agreement with the literature data.[37] This may be attributed to the enhanced interfacial chemical interaction and increased coverage of titania with Ag_2S.[38] This can also explain the fact that although 45-Ag_2S/gTiNT has a lower energy bandgap than

25-Ag_2S/gTiNT, the latter one exhibits better photoelectrochemical activity. Interestingly, contradictory results were obtained for modified fTiNT electrodes, namely the values of energy bandgaps increase with the cycle number. It should be in here mentioned, that apart of the changes in nanotubes diameter, the purity of Ti influences on the wall thickness and it was already reported that it rises with higher purity of layer out of which nanotubes were grown.[39] Similar effect was observed in this work – see Fig. 4(a) and (b).

Therefore, taking into account optical properties, better photoelectrochemical performance of Ag_2S-coated electrodes under visible light is expected compared to uncoated TiNT. As it will be shown, although 45-Ag_2S/gTiNT absorbs more light than 25-Ag_2S/gTiNT, it does not mean that the sample has the highest photoelectrochemical activity (Table 1).

3.2.3 Chemical structure.

The chemical states of titanium Ti 2p (Fig. 5a), oxygen O 1s (b), carbon C 1s (c), silver Ag 3d (d), and sulfur S 2p (e) were determined using X-ray photoelectron spectroscopy analysis. Table S3† presents the percentage contribution and binding energy of electrodes. A detailed interpretation of all recorded spectra was provided based on the peak fitting and deconvolution procedure. The 25-Ag_2S/gTiNT and 25-Ag_2S/fTiNT electrodes were selected for analysis due to their high photoelectrochemical activity as well as the 45-Ag_2S/gTiNT electrode which exhibits the best activity towards oxygen evolution reaction in alkaline electrolyte. The XPS spectrum of Ti 2p is shown in Fig. 4a with all samples, both on glass and on titanium foil, exhibits a peak doublet. For the pure fTiNT sample, the binding energies are 458.48 and 464.18 eV, corresponding to the spin–orbital splitting of Ti $2p_{3/2}$ and Ti $2p_{1/2}$. These values were assigned to titanium in the +4 oxidation state, indicating a bonding consistent with stoichiometric TiO_2.[40] Between the glass and foil samples, a slight shift towards higher energies, less than 0.3 eV for the glass sample, has been observed. This result might be correlated with shift observed in Raman spectra due to a lack of impurities (see Fig. 1e). Additionally, it was observed that spectra of samples modified with silver sulfide show slight asymmetry in the peaks. This shift can be correlated with additional modifications of the samples under the influence of UV radiation coupled with ozone generation[41,42] or annealing in argon atmosphere.[43] The deconvolution of the O 1s spectrum (Fig. 5b) yielded three peaks at binding energies of 529.98, 531.18, and 532.58 eV. The first peak is, associated with Ti–O bonding from the TiO_2 crystalline lattice.[44] The next maximum corresponds to hydroxyl groups, which occur on the sample's surface,[45] or oxygen vacancies and excess electron density in Ti.[46] The last peak can be assigned to carboxyl groups.[47] For the C 1s spectrum shown in Fig. 5c, three peaks were assigned with binding energy values of 284.58, 286.08, and 288.38 eV. The C 1s peak at approximately 284.58 eV is typically attributed to residual C in the precursor organic compound, which has adsorbed onto the surface of the photocatalyst, specifically to C–C bonds. The subsequent peaks at 286.08 and 288.38 eV are assigned, respectively, to C–O and O–C═O bonds, specifically to carbonate species present from electrolyte.[48,49] Next, deconvolution of the Ag 3d spectrum (Fig. 5d) was performed, assigning a doublet of peaks. The first maximum at 367.38 eV is associated with $3d_{5/2}$, and the second, with a value of 373.38 eV, originating from $3d_{3/2}$. These maxima indicate the presence of the Ag^+ valence state in the form of Ag_2S.[50,51] Additionally, a shift of the maximum can be observed for the sample made on the foil, but smaller than 0.3 eV. Lastly, deconvolution was performed for the S 2p spectrum (Fig. 5e). A doublet was detected, indicating sulfur bonding with only one element. In the observed spectra, two maxima were found: 160.38 and 161.58 eV, representing the spin–orbit pair $2p_{3/2}$ and $2p_{1/2}$ in metal sulfides, providing evidence of Ag_2S [50] though with the low sulfur signal for the fTiNT samples, more quantitative analysis is not possible. As the number of SILAR cycles increases, the percentage of sulfur increases from 0.84 at% to 1.75 at%, and the percentage of silver from 1.54 at% to 2.07 at% for samples on glass substrates.

Table 1 Energy bandgap values estimated for modified gTiNT and fTiNT samples

Sample name	Energy bandgap (eV)	Sample name	Energy bandgap (eV)
5-Ag_2S/gTiNT	2.69	5-Ag_2S/fTiNT	2.42
25-Ag_2S/gTiNT	2.65	25-Ag_2S/fTiNT	2.59
45-Ag_2S/gTiNT	1.74	45-Ag_2S/fTiNT	2.9
gTiNT	2.96	fTiNT	2.95

3.2.4 Electrochemical and photoelectrochemical activity

Electrochemical activity in 0.5 M Na_2SO_4. The electrochemical activity of Ag_2S-coated gTiNT and fTiNT electrodes first was tested using cyclic voltammetry in 0.5 M Na_2SO_4. The results are presented in the Fig. 6. When the electrode is immersed in the solution, OH^- groups adsorb on Ag_2S. During the anodic potential scan silver oxides are formed on the surface ((A1), (A2) and (A3)) leading to the release of sulfur ions, whereas, during the reverse scan silver oxides are reduced ((C2) and (C1)):[52]

$$2[Ag(OH)_2]_{aq}^- \rightarrow Ag_2O + H_2O + 2OH^- \tag{A1}$$

$$Ag_2O + 2OH^- \rightarrow 2AgO + H_2O + 2e^- \tag{A2}$$

$$2AgO + 2OH^- \rightarrow Ag_2O_3 + H_2O + 2e^- \tag{A3}$$

$$2AgO + H_2O + 2e^- \rightarrow Ag_2O + 2OH^- \tag{C2}$$

$$Ag_2O + H_2O + 2e^- \rightarrow 2Ag + 2OH^-. \tag{C1}$$

The 5-Ag_2S-coated gTiNT and fTiNT electrodes are not characterized by any significant anodic or cathodic peaks from the above list of proposed reactions (see Fig. 6a and b). However, as the number of cycles increases, an anodic peak ascribed as (A1) at *ca.* −0.6 V *vs.* Ag/AgCl/0.1 M KCl assigned to oxidation of Ag to Ag_2O is characterized by higher current density values. The reduction peak assigned as (C1) at *ca.* −0.9 V behaves analogously. Considering the (A2) and (A3) peaks, which are the most visible for the 25-Ag_2S/gTiNT electrode,

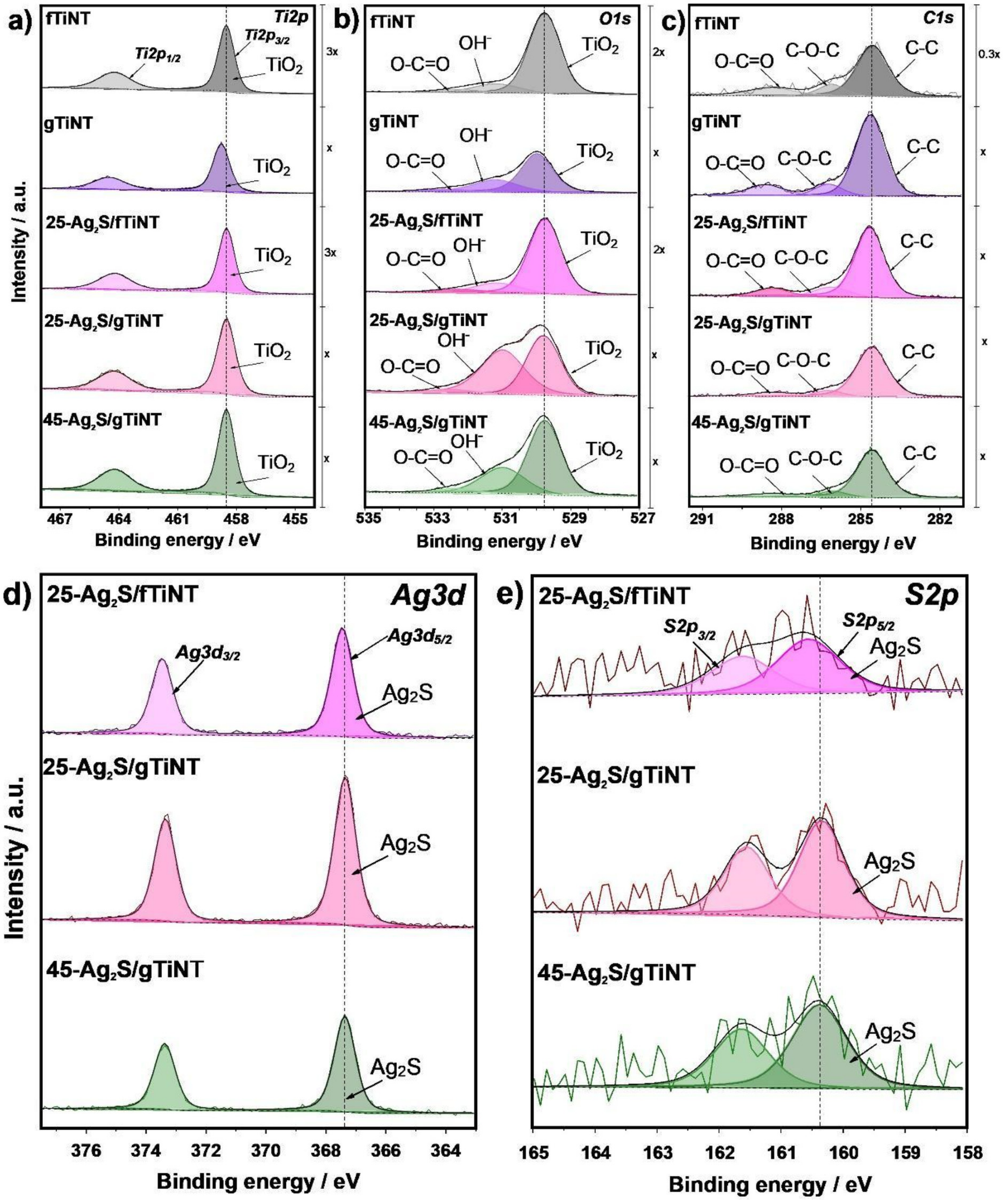

Fig. 5 XPS high resolution spectra registered for the fTiNT, gTiNT, 25-Ag_2S/fTiNT, 25-Ag_2S/gTiNT, 45-Ag_2S/gTiNT (a) Ti 2p, (b) O 1s, (c) C 1s, (d) Ag 3d, (e) S 2p.

such peaks can appear broader or less pronounced because of differences between the diameter and aggregations of Ag NPs.[53] The photoelectrochemical activity was tested by linear voltammetry under chopped visible light illumination for wavelengths above 420 nm in 0.5 M Na_2SO_4. It can be clearly seen than activity differs between the samples on glass and foil substrates (Fig. 6c and d). The highest photocurrent of 21 μA cm^{-2} registered at 0.4 V *vs.* Ag/AgCl/0.1 M KCl was obtained for the 25-Ag_2S/gTiNT electrode. This activity is correlated with the presence of silver oxides in various oxidation states as Ag_2O, AgO, and Ag_2O_3. According to Sakar *et al.*[54] and Allen *et al.*[55] Ag_2O, AgO, and Ag_2O_3 is characterized by a

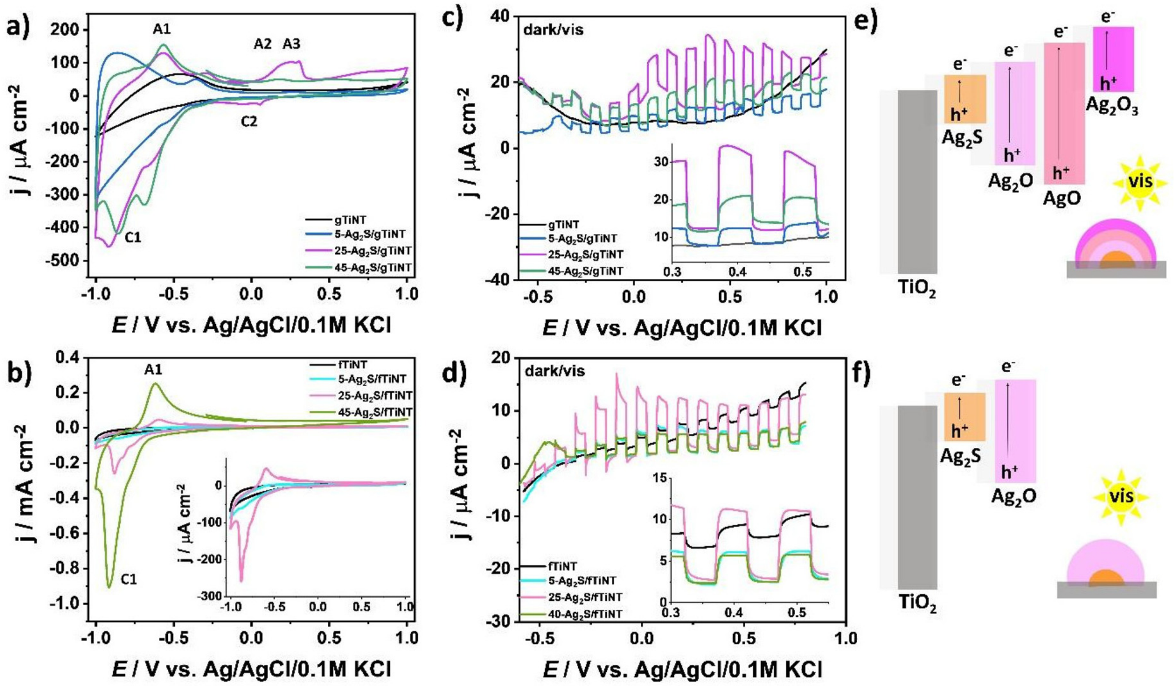

Fig. 6 Cyclic voltammetry curves for (a) 5-, 25-, 45-Ag_2S/gTiNT, bare gTiNT, (b) 5-, 25-, 40-Ag_2S/fTiNT, bare fTiNT (50 mV s^{-1}) and linear voltammetry curves for (c) 5-, 25-, 45-Ag_2S/gTiNT, bare gTiNT, (d) 5-, 25-, 40-Ag_2S/fTiNT, bare fTiNT under visible light illumination registered in 0.5 M Na_2SO_4 at a scan rate of 10 mV s^{-1} and (e) energy band diagram for the 25-Ag_2S/gTiNT electrode, (f) energy band diagram for the 25-Ag_2S/fTiNT electrode.

bandgap energy of 1.5 eV, 2.25 eV, and 0.96 eV, respectively. Therefore, the combination of three oxides where silver(III) oxide has the smallest bandgap energy (Fig. 6e) is more favourable for photocurrent generation in contrast to presence of silver(I) oxide which has *ca.* 2 times higher bandgap (Fig. 6f). As can be seen, the most pronounced (A1), (A2), and (A3) peaks on CV were registered for electrode with the highest photoelectrochemical activity. In the case of 25-Ag_2S/fTiNT electrode with the presence of the (A1) peak assigned to silver (I) oxide, the photocurrent density at 0.4 V is equal to 8 μA cm^{-2} which is *ca.* 3 times lower current than for samples coated by Ag_2S in the same conditions but on gTiNT.

The 25Ag_2S/gTiNT electrode was exposed to light of different wavelengths to track its photoresponse in different light conditions. As a source of light, we used a LED revolver with light power in the range of 30 to 100 mW depending on the average wavelength. Fig. S4† presents photocurrent *vs.* time for different wavelengths recorded at +0.5 V and +1.0 V *vs.* Ag/AgCl/0.1 M KCl. The highest photocurrent was recorded for wavelength 373 nm, followed by 405 and 424 nm. As the wavelength increased, the photocurrent value decreased in accordance with the absorbance profile. It is worth mentioning that the higher the potential, the greater the contribution of the shortest investigated wavelength, namely 373 nm, to the overall photocurrent since the material absorbs light near the UV range.

Analysis of electrode composition. In order to characterize the silver sulfides and silver oxides, Raman spectroscopy was used to study the electrodes before and after cyclic voltammetry measurements carried out in 0.5 M Na_2SO_4 (Fig. 7). The combination of Raman and CV is an advantageous approach for comprehensive study of silver compounds allowing monitoring of structural changes during electrochemical processes. All changes observed in Raman spectra can be correlated with the electrochemical behaviour offering insight into the mechanism and kinetics of silver containing compounds that transform upon electrochemical tests. According to Fig. 1e the 145, 394, 516, and 634 cm^{-1} bands correspond to anatase TiO_2 phase. Therefore, Tables S4 and S5† present only the location of Raman bands for compounds with silver species. First, the peak located at 145 cm^{-1} is assigned to the presence of the anatase phase that overlaps with the Ag_2SO_3 band.[56] The measurements were performed in electrolyte containing SO_4^{2-} ions which may be reduced to SO_3^{2-} by some reducing agent during the CV scans. As shown by XPS analysis, the 25-Ag_2S/gTiNT and 45-Ag_2S/gTiNT electrodes are composed of Ag_2S. Therefore, it can be assumed Ag^+ can act as reducing agent for SO_4^{2-} where Ag_2S can be oxidized to Ag_2O and AgO.[58] Subsequently non-oxidized Ag^+ can bind with SO_3^{2-}. The Ag–S bands can be found at 205, 225, 243, 250, and 276 cm^{-1}.[57,58] In the case of the 25-Ag_2S/gTiNT electrode after 3 and 10 CV cycles all remain well visible on Raman spectra. For the 45-Ag_2S/gTiNT electrode bands at 205 and 243 cm^{-1} disappear after 10 cycles and a small new band at 276 cm^{-1} developed. This result indicates that some silver sulfides are preserved on the surface of the 25-Ag_2S/gTiNT electrode after 10 cycles. This

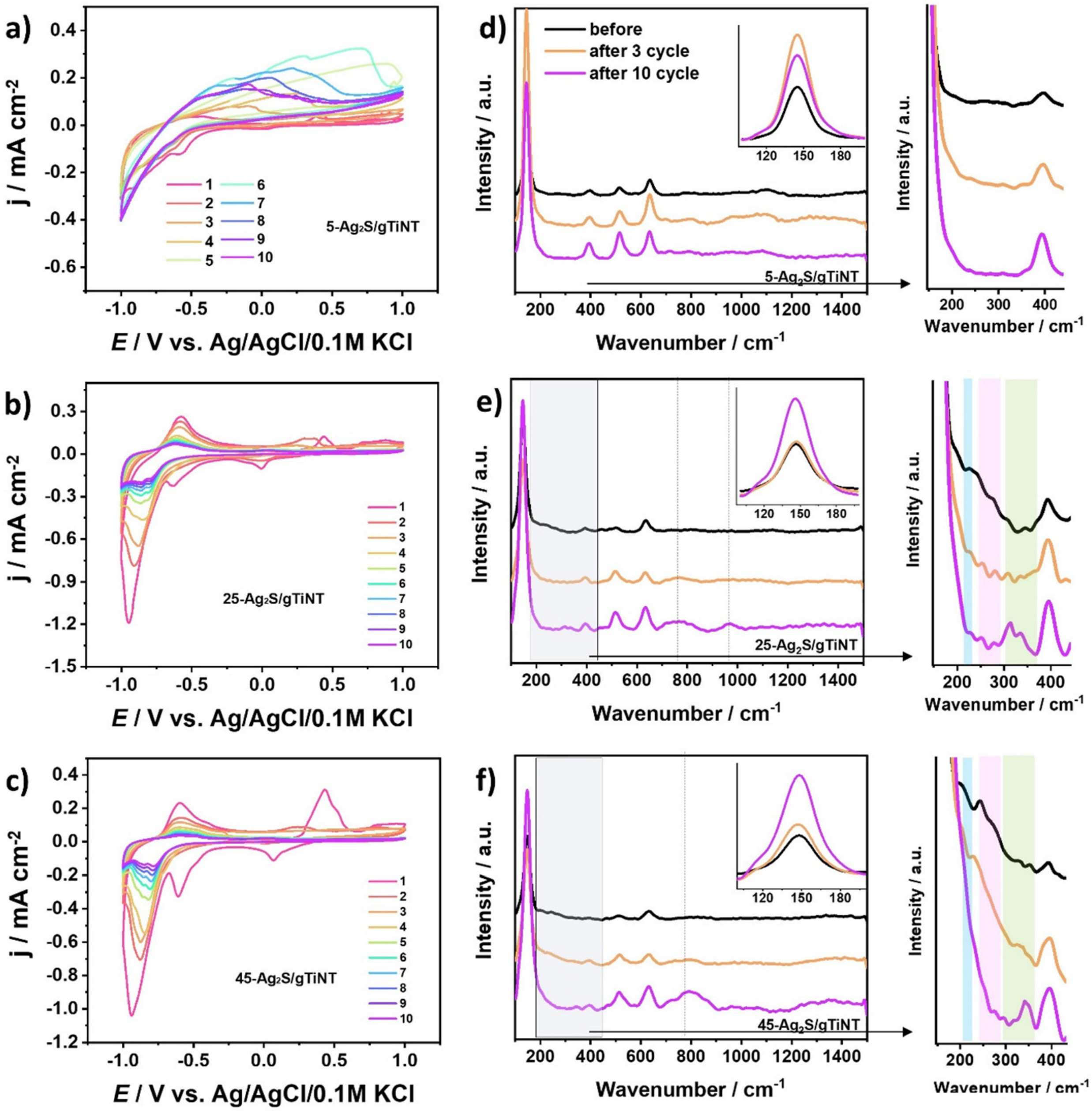

Fig. 7 Cyclic voltammetry curves of (a) 5-Ag_2S/gTiNT, (b) 25-Ag_2S/gTiNT, (c) 45-Ag_2S/gTiNT and Raman spectra before CVs and after 3 or 10 CVs cycles for (d) 5-Ag_2S/gTiNT, (e) 25-Ag_2S/gTiNT, (f) 45-Ag_2S/gTiNT in 0.5 M Na_2SO_4 electrolyte (scan rate 50 mV s^{-1}). All the graphs on the right are insets of the Raman graphs.

is consistent with the photoelectrochemical results where the best photoelectrochemical activity was obtained for samples with 25 SILAR deposition cycles. Furthermore, Raman bands located at 295, 310, 325, 340, and 350 cm^{-1} are assigned to Ag–O, whereas 790 cm^{-1} corresponds to O–Ag–O.[58] As CV cycles increases in number, bands on Raman spectra attributed to silver oxide becomes more and more intense.

Electrochemical activity in 0.5 M NaOH. The electrochemical activity of Ag_2S-coated TiO_2 nanotubes fabricated on glass and foil substrates were tested by cyclic voltammetry not only in 0.5 M Na_2SO_4 but also in 0.5 M NaOH. The results are presented in Fig. 8. The anodic peaks are associated with oxidation of Ag to Ag_2O and Ag_2O to AgO named (A1) and (A2), respectively. Whereas cathodic peaks correspond to reduction of AgO to Ag_2O and Ag_2O to Ag described as (C2) and (C1), respectively. It should be highlighted that electrodes fabricated on ITO exhibit higher currents than those obtained on Ti foil, especially towards OER. The tendency in both cases for Ag_2S-coated gTiNT and fTiNT is similar, which means that as the number of SILAR cycles increases the current density value

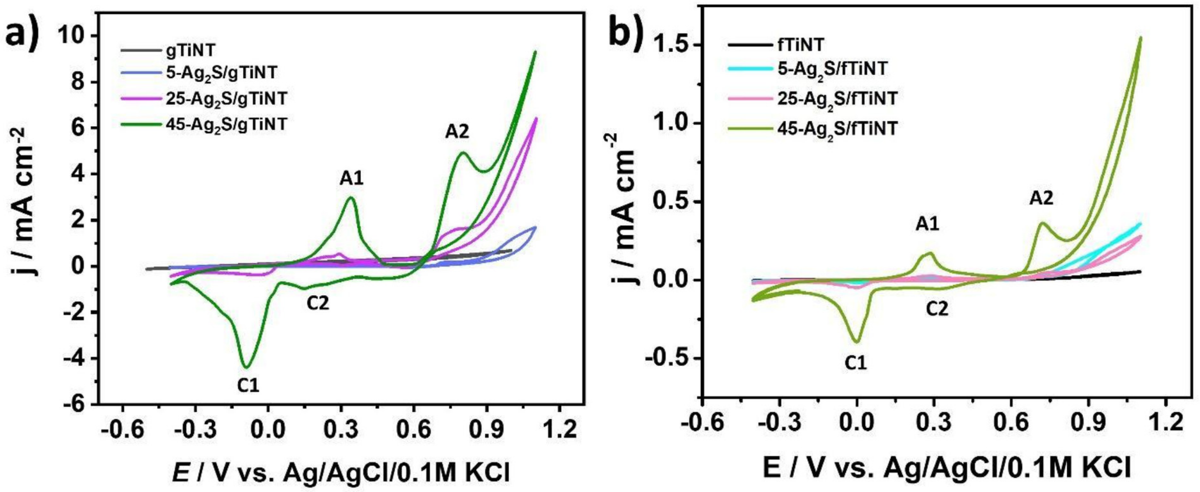

Fig. 8 Cyclic voltammetry curves for (a) Ag_2S-coated and non-coated gTiNT and (b) Ag_2S-coated and non-coated fTiNT in 0.5 M NaOH electrolyte (scan rate 50 mV s^{-1}).

increases. The highest current density of 9.3 mA cm^{-2} registered at +1.1 V *vs.* Ag/AgCl/0.1 M KCl was obtained for the 45-Ag_2S/gTiNT electrode. It should be underlined that the 45-Ag_2S/gTiNT electrode reached *ca.* 6 times higher current density associated with activity towards OER at +1.1 V than the 45-Ag_2S/fTiNT electrode. As was already underlined by XPS analysis as well as Raman spectra, Ag_2S species are present on the electrode before the immersion in the electrolyte and electrochemical measurements. However, after 10 CV cycles, new compounds as Ag_2O and AgO arose on the surface. Therefore, it can be claimed that not only metal sulfides, but also metal oxides can still be responsible for the overall catalytic performance.[59] The first three cycles from the CV measurement for Ag_2S-coated gTiNT and fTiNT are in Fig. S5.† Additionally, the results for the 45-Ag_2S/gTiNT in 0.1, 0.5, and 1 M NaOH electrolytes are presented in Fig. S6.†

Inspection of electrode stability. In order to explore the activity of silver sulfides and silver oxides towards OER and their stability in 0.5 M NaOH, Raman spectroscopy was combined with cyclic voltammetry measurements (Fig. 9). The 25-Ag_2S/gTiNT and 45-Ag_2S/gTiNT were chosen for further analysis because of their catalytic activity. Focusing on CV, 10 curves were recorded for the 25-Ag_2S/gTiNT electrode. It can be seen that anodic and cathodic peaks related to oxidation and reduction of silver oxides disappear. However, the electrode is still active towards OER. Furthermore, the current density value registered for the 25-Ag_2S/gTiNT at +1.1 V *vs.* Ag/AgCl/0.1 M KCl for 5, 6, 7, 8, 9, and 10 cycle is the same, while between 1 and 5 cycles slight differences can be observed. The variations between current density at those potential conditions is stopped together with the absence of redox peaks originating from silver oxides. The Raman spectral peaks for the 25-Ag_2S/gTiNT located at 225, 240, 255, 270, and 280 cm^{-1} are assigned to the Ag–S bond.[48,57] However, after 10 cycles those peaks disappear or become less pronounced but simultaneously the peak located at 145 cm^{-1} becomes more intense. This observation can be related with a silver lattice vibrational phase transition.[60] In the case of 45-Ag_2S/gTiNT this peak become even more prominent which can be correlated with the higher number of SILAR cycles and thus the amount of Ag_2S on the surface. As can be seen in Fig. 9b for 25-Ag_2S/gTiNT, the peaks attributed to faradaic reaction occurring at the potential associated with silver oxide disappear, indicating instability of the electrode material, whereas, for 45-Ag_2S/gTiNT such peaks do not change in position or intensity for numerous cycles. Therefore, it can be claimed that for 25-Ag_2S/gTiNT, Ag_2S is the main catalyst for OER and for 45-Ag_2S/gTiNT the activity is additionally enhanced by the presence of silver oxides formed during the measurement.[58] The most visible changes in the Raman spectra, namely peaks which are not observed before electrochemical measurements but appear after 10 cycles, are at 790, 980 and 1077 cm^{-1} for O–Ag–O, S–O and Ag–O bonds.[58,61]

The stability of electrochemical performance was verified by chronoamperometry measurements recorded at +1.0 V *vs.* Ag/AgCl/0.1 M KCl and the multicyclic voltammetry where the potential was changed from −0.4 to +1.1 V *vs.* Ag/AgCl/0.1 M KCl (see Fig. S7†). As one can observe the electrode performance is stable throughout the whole CA measurement duration. Sharp peaks appearing cyclically are due to the gas bubbles that are formed at the applied potential on the electrode surface. The evolution of oxygen bubbles proceeds and in consequence appearing gas bubbles at the electrode/electrolyte interface change the contact surface area between the electrode and electrolyte. Taking into account CV measurements from cycle to cycle the redox peaks diminish and finally at the 50th cycle we do not observe any oxidation and reduction signals that were noted at the first CV run. This change occurs due to the release of sulfur ions, and oxidation of all silver as described in Table S5.†

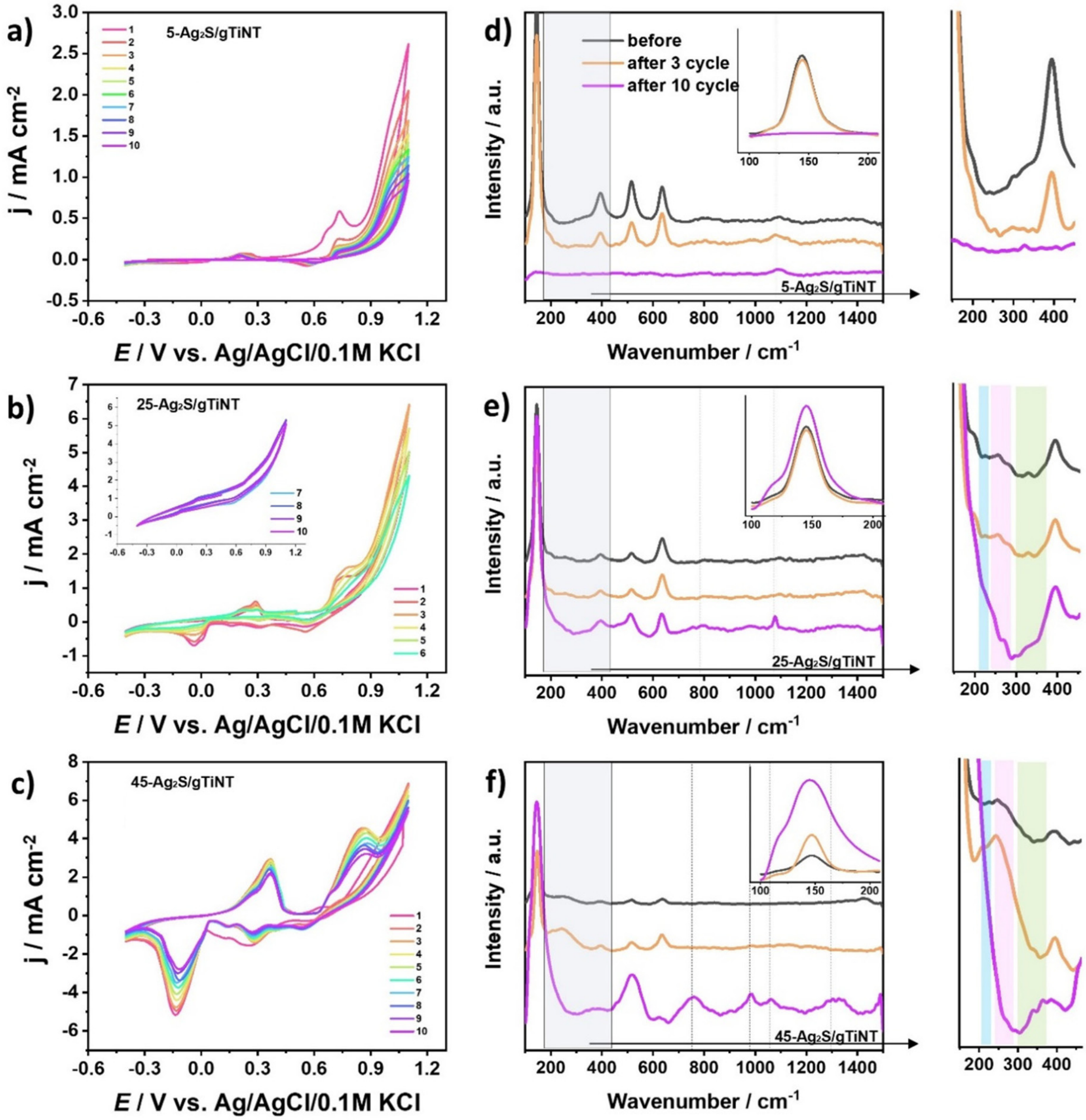

Fig. 9 Cyclic voltammetry curves of (a) 5-Ag_2S/gTiNT, (b) 25-Ag_2S/gTiNT, (c) 45-Ag_2S/gTiNT and Raman spectra before CVs and after 3 or 10 CVs cycles for (d) 5-Ag_2S/gTiNT, (e) 25-Ag_2S/gTiNT, (f) 45-Ag_2S/gTiNT in 0.5 M NaOH electrolyte (scan rate 50 mV s^{-1}). All the graphs on the right are insets of the Raman graphs.

4. Conclusions

We showcase how adding silver sulfide to titanium dioxide nanotubes affects their shape, structure, and optical properties, as well as photoelectrochemical and electrochemical activity. This study explores these effects when the NT are grown on ITO substrates with a sputtered Ti layer or on Ti foil. The successive ionic layer adsorption and reaction method with the use of silver and sulfur precursors enables the formation of silver sulfide species inside the nanotubes. It has been shown that Ag_2S-coated transparent TiO_2 nanotubes exhibit better photoelectrochemical activity under visible light illumination and activity towards the oxygen evolution reaction than if the non-transparent material was used as a substrate. In both cases, the highest photocurrent was obtained by electrodes coated with 25 SILAR cycles while nanostructures fabricated on ITO substrates obtained *ca.* 3 times higher currents. In the case of Ag_2S transparent samples, a combination of Ag_2S, Ag_2O, AgO, and Ag_2O_3 compounds took part in the photoelectrochemical process. Whereas for Ag_2S deposited on TiO_2 nanotubes and Ti foil only Ag_2S and Ag_2O were involved in photocurrent generation. The highest activity towards OER was obtained by transparent nanotubes coated by 45 SILAR cycles and reached of 9.3 mA cm^{-2} at 1.1 V *vs.* Ag/AgCl/0.1 M

KCl which is six times higher than the non-transparent material also obtained *via* anodization of Ti foil. The significant catalytic activity was enhanced by a synergetic effect between silver sulfide and silver oxides. Considering both structural and electrochemical data, transparent TiO_2 nanotubes are characterised by more uniformly distributed nanotubes with smaller diameter and higher purity with lower charge transfer resistance than TiO_2 nanotubes on Ti foil. Ag_2S deposition improved the overall electrochemical performance of transparent electrodes and warrants further exploration.

Data availability

The data supporting this article have been included as part of the ESI.†

Conflicts of interest

There are no conflicts to delare.

Acknowledgements

This work is financially supported by the National Science Centre (Poland): Grant no. 2020/39/I/ST5/01781 and by the Deutsche Forschungsgemeinschaft (DFG – German Research Foundation) for project number 465220299. KED and SPH acknowledge scholarship funding from the Deutsche Bundesstiftung Umwelt (DBU – German Federal Environmental Foundation).

References

1 S. Fawzy, A. I. Osman, J. Doran and D. W. Rooney, Strategies for mitigation of climate change: a review, *Environ. Chem. Lett.*, 2020, **18**, 2069–2094.

2 Y. Yan, B. Y. Xia, B. Zhao and X. Wang, A review on noble-metal-free bifunctional heterogeneous catalysts for overall electrochemical water splitting, *J. Mater. Chem. A*, 2016, **4**, 17587–17603.

3 S. Chandrasekaran, L. Yao, L. Deng, C. Bowen, Y. Zhang, S. Chen, Z. Lin, F. Peng and P. Zhang, Recent advances in metal sulfides: from controlled fabrication to electrocatalytic, photocatalytic and photoelectrochemical water splitting and beyond, *Chem. Soc. Rev.*, 2019, **48**, 4178–4280.

4 J. A. Nasir, Z. Rehman, S. N. A. Shah, A. Khan, I. S. Butler and C. R. A. Catlow, Recent developments and perspectives in CdS-based photocatalysts for water splitting, *J. Mater. Chem. A*, 2020, **8**, 20752–20780.

5 X. Sun, Z. Chen, Y. Shen, J. Lu, Y. Shi, Y. Cui, F. Guo and W. Shi, Plasmonic coupling-boosted photothermal nanoreactor for efficient solar light-driven photocatalytic water splitting, *J. Colloid Interface Sci.*, 2023, **652**, 1016–1027.

6 Y. Yong, R. W. Crisp, J. Gu, B. D. Chernomordik, G. F. Pach, A. R. Marshall, J. A. Turner and M. C. Beard, Multiple exciton generation for photoelectrochemical hydrogen evolution reactions with quantum yields exceeding 100%, *Nat. Energy*, 2017, **2**, 17052.

7 M. Wang, L. Zhang, Y. He and H. Zhu, Recent advances in transition-metal-sulfide-based bifunctional electrocatalysts for overall water splitting, *J. Mater. Chem. A*, 2021, **9**, 5320–5363.

8 X. Ma, W. Zhang, Y. Deng, C. Zhong, W. Hu and X. Han, Phase and composition controlled synthesis of cobalt sulfide hollow nanospheres for electrocatalytic water splitting, *Nanoscale*, 2018, **10**, 4816–4824.

9 S. Shit, W. Jang, S. Bolar, N. C. Murmu, H. Koo and T. Kuila, Effect of solvent ratio (ethylene glycol/water) on the preparation of iron sulfide electrocatalyst and its activity towards overall water splitting, *ChemElectroChem*, 2019, **6**, 3199–3208.

10 S. Shen and Q. Wang, Rational Tuning the Optical Properties of Metal Sulfide Nanocrystals and Their Applications, *Chem. Mater.*, 2012, **25**, 1166–1178.

11 Y. Shiga, N. Umezawa, N. Srinivasan, S. Koyasu, E. Sakai and M. Miyauchi, A metal sulfide photocatalyst composed of ubiquitous elements for solar hydrogen production, *Chem. Commun.*, 2016, **52**, 7470–7473.

12 F. C. M. Spoor, G. Grimaldi, C. Delerue, W. H. Evers, R. W. Crisp, P. Geiregat, Z. Hens, A. J. Houtepen and L. D. A. Siebbeles, Asymmetric Optical Transitions Determine the Onset of Carrier Multiplication in Lead Chalcogenide Quantum Confined and Bulk Crystals, *ACS Nano*, 2018, **12**, 4796–4802.

13 V. Mauritz, K. E. Dehm, S. P. Hager and R. W. Crisp, Colloidal nanocrystal synthesis of alkaline earth metal sulfides for solution-processed solar cell contact layers, *Z. Kristallogr. – Cryst. Mater.*, 2023, **238**, 295–300.

14 H. Roshan, A. Mirzaei, T. Kaewmaraya, T. Hussain and R. Brescia, Broadband photo detection using metal excess silver sulfide nanocrystals, *J. Alloys Compd.*, 2023, **939**, 168754.

15 H. Shen, X. Jiao, D. Oron, J. Li and H. Lin, Efficient electron injection in non-toxic silver sulfide (Ag_2S) sensitized solar cells, *J. Power Sources*, 2013, **240**, 8–13.

16 S. Wageh, A. A. Al-Ghamdi, A. Numan and J. Iqubal, Silver sulfide nanoparticles incorporated into graphene oxide: an efficient electrocatalyst for the oxygen reduction reaction, *J. Mater. Sci.: Mater. Electron.*, 2020, **31**, 8127–8135.

17 Z. Zhang, X. Li, C. Zhong, N. Zhao, Y. Deng, X. Han and W. Hu, Spontaneous Synthesis of Sliver Nanoparticles Decorated Transition-Metal Hydroxides for Enhanced Oxygen Evolution Reaction, *Angew. Chem., Int. Ed.*, 2020, **59**, 7245–7250.

18 I. A. Ezenwa, N. A. Okereke and N. I. Egwunyenga, Optical Properties of Chemical Bath Deposited Ag_2S Thin Films, *Int. J. Sci. Technol.*, 2012, **2**, 101–106.

19 X. Li, G. Zhu, L. Xiao, Y. Liu, Z. Ji, X. Shen and S. A. Shah, Loading of Ag on Fe-Co-S/N-doped carbon nanocomposite

to achieve improved electrocatalytic activity for oxygen evolution reaction, *J. Alloys Compd.*, 2018, **773**, 40–49.

20 W. Lipińska, K. Grochowska, J. Ryl, J. Karczewski and K. Siuzdak, Influence of annealing atmosphere on photoelectrochemical activity of TiO_2 nanotubes modified with AuCu nanoparticles, *ACS Appl. Mater. Interfaces*, 2021, **13**, 52967–52977.

21 W. Lipińska, K. Grochowska, J. Karczewski, E. Coy and K. Siuzdak, Electrocatalytic oxidation of methanol, ethylene glycol and glycerine in alkaline media on TiO_2 nanotubes decorated with AuCu nanoparticles for an application in fuel cells, *J. Mater. Sci.*, 2022, **57**, 13345–13361.

22 A. S. Bondarenko and G. A. Ragoisha, Variable Mott-Schottky plots acquisition by potentiodynamic electrochemical impedance spectroscopy, *J. Solid State Electrochem.*, 2005, **9**, 845–849.

23 V. Sivaprakash and R. Narayanan, Synthesis of TiO_2 nanotubes via electrochemical anodization with different water content, *Mater. Today: Proc.*, 2020, **37**, 142–146.

24 K. Grochowska, N. Nedyalkov, J. Karczewski, Ł. Haryński, G. Śliwiński and K. Siuzdak, Anodic titania nanotubes decorated with gold nanoparticles produced by laser-induced dewetting of thin metallic films, *Sci. Rep.*, 2020, **10**, 20506.

25 A. Hankova, A. Kuzminova, J. Hanus, P. Sezemsky, R. Simerova, V. Stranak, K. Grochowska, D. S. Kouao, K. Siuzdak, M. Prochazka, T. Kosutova and O. Kylian, TiO_2/Ag nanostructured coatings as recyclable platforms for surface-enhanced Raman scattering detection, *Surf. Interfaces*, 2022, **35**, 102441.

26 H. Li, G. Wang, J. Niu, E. Wang, G. Niu and C. Xie, Preparation of TiO_2 nanotube arrays with efficient photocatalytic performance and super-hydrophilic properties utilizing anodized voltage method, *Results Phys.*, 2019, **14**, 102499.

27 S. Senthilkumar, M. Ashok, L. Kashinath, C. Sanjeeviraja and A. Rajendran, Phytosynthesis and Characterization of TiO_2 Nanoparticles using Diospyros ebenum Leaf Extract and their Antibacterial and Photocatalytic Degradation of Crystal Violet, *Smart Sci.*, 2017, **6**, 1–9.

28 B. Munirathinam and L. Neelakantan, Titania nanotubes from weak organic acid electrolyte: Fabrication, characterization and oxide film properties, *Mater. Sci. Eng., C*, 2015, **49**, 567–578.

29 K. Siuzdak, M. Szkoda, A. Lisowska-Oleksiak, J. Karczewski and J. Ryl, Highly stable organic–inorganic junction composed of hydrogenated titania nanotubes infiltrated by a conducting polymer, *RSC Adv.*, 2016, **6**, 33101–33110.

30 D. P. Oyarzún, R. Córdova, O. E. Linarez Pérez, E. Muñoz, R. Henríquez, M. López Teijelo and H. Gómez, Morphological, electrochemical and photoelectrochemical characterization of nanotubular TiO_2 synthetized electrochemically from different electrolytes, *J. Solid State Electrochem.*, 2010, **15**, 2265–2275.

31 S. Pausova, S. Kment, M. Zlamal, M. Baudys, Z. Hubicka and J. Krysa, Transparent nontubular TiO_2 photoanodes grown directly on FTO substrates, *Molecules*, 2017, **22**, 775.

32 T. Hoseinzadeh, Z. Ghorannevis, M. Ghorannevis, A. H. Sari and M. K. Salem, Effects of various applied voltages on physical properties of TiO_2 nanotubes by anodization method, *J. Theor. Appl. Phys.*, 2017, **11**, 243–248.

33 A. Al-Haddad, Z. Wang, R. Xu, H. Qi, R. Vellacheri, U. Kaiser and Y. Lei, Dimensional dependence of the optical absorption band edge of TiO_2 nanotube arrays beyond the quantum effect, *J. Phys. Chem. C*, 2015, **119**, 16331–16337.

34 G. L. Chiarello, A. Zuliani, D. Ceresoli, R. Martinazzo and E. Selli, Exploiting the Photonic Crystal Properties of TiO_2 Nanotube Arrays To Enhance Photocatalytic Hydrogen Production, *ACS Catal.*, 2016, **6**, 1345–1353.

35 L. Cheng, H. Ding, C. Chen and N. Wang, Ag_2S/Bi_2S_3 co-sensitized TiO_2 nanorod arrays prepared on conductive glass as a photoanode for solar cells, *J. Mater. Sci.: Mater. Electron.*, 2016, **27**, 3234–3239.

36 J. Wawrzyniak, K. Grochowska, J. Karczewski, P. Kupracz, J. Ryl, A. Dołęga and K. Siuzdak, The geometry of free-standing titania nanotubes as a critical factor controlling their optical and photoelectrochemical performance, *Surf. Coat. Technol.*, 2020, **389**, 125628.

37 A. Badawi, Effect of the non-toxic Ag_2S quantum dots size on their optical properties for environment-friendly applications, *Phys. E*, 2019, **109**, 107.

38 S. Ghafoor, S. Ata, N. Mahmood and S. N. Arshad, Photosensitization of TiO_2 nanofibers by Ag_2S with the synergistic effect of excess surface Ti^{3+} states for enhanced photocatalytic activity under simulated sunlight, *Sci. Rep.*, 2017, **7**, 254.

39 S. B. Taieb, I. B. Assaker, A. Bardaoui, M. Gannouni, A. Souissi, S. Nowak and R. Chtourou, Correlation between Titanium foil substrate purity and TiO_2 NTs; physical and electrochemical properties for enhanced photoelectrochemical applications, *Int. J. Hydrogen Energy*, 2016, **41**, 6230.

40 J. F. Moulder, W. F. Stickle, P. E. Sobol and K. D. Bomben, in *Handbook of X-ray Photoelectron Spectroscopy*, ed. J. Chastain, Perkin-Elmer Corporation, 1992.

41 C. Dawo, M. A. Afroz, P. K. Iyer and H. Chaturvedi, Optimization and effect of UV-ozone exposure of electron transport layer on the efficiency of the dye-sensitized solar cells, *arxiv physics*, 2020, **https://arxiv.org/abs/2002.12071**.

42 S. Ghafoor, S. Ata, N. Mahmood and S. N. Arshad, Photosensitization of TiO_2 nanofibers by Ag_2S with the synergistic effect of excess surface Ti^{3+} states for enhanced photocatalytic activity under simulated sunlight, *Sci. Rep.*, 2017, **7**, 1–10.

43 W. Lipinska, Z. Bielan, A. Witkowska, J. Karczewski, K. Grochowska, E. Partyka-Jankowska, T. Sobol, M. Szczepanik and K. Siuzdak, Insightful studies of AuCu nanostructures deposited on Ti platform: Effect of rapid thermal annealing on photoelectrochemical activity supported by synchrotron radiation studies, *Appl. Surf. Sci.*, 2023, **638**, 158048.

44 H. Kiziltas, Fabrication and characterization of photoelectrode B–Co/TiO_2 nanotubes for effective photoelectrochemical degradation of rhodamine B, *Opt. Mater.*, 2022, **123**, 111926.

45 H. Li, Z. Yang, X. Cui, Y. Li, P. Zhang and J. Li, A highly efficient $In_2S_3/Ag_2S/TiO_2$ NTAs photoelectrodes for photocathodic protection of Q235 carbon steel under visible light, *Nanotechnology*, 2022, **34**, 045705.

46 K. H. Park and M. Dhayal, High efficiency solar cell based on dye sensitized plasma treated nano-structured TiO_2 films, *Electrochem. Commun.*, 2009, **11**, 75–79.

47 X. Zhang, Y. Chen, Y. Xiao, W. Zhou, G. Tian and H. Fu, Enhanced charge transfer and separation of hierarchical hydrogenated TiO_2 nanothorns/carbon nanofibers composites decorated by NiS quantum dots for remarkable photocatalytic H_2 production activity, *Nanoscale*, 2018, **10**, 4041–4050.

48 Z. Wu, F. Dong, W. Zhao, H. Wang, Y. Liu and B. Guan, The fabrication and characterization of novel carbon doped TiO_2 nanotubes, nanowires and nanorods with high visible light photocatalytic activity, *Nanotechnology*, 2009, **20**, 235701.

49 W. Ren, Z. Ai, F. Jia, L. Zhang, X. Fan and Z. Zou, Low temperature preparation and visible light photocatalytic activity of mesoporous carbon-doped crystalline TiO_2, *Appl. Catal., B*, 2007, **69**, 138–144.

50 Q. Wang, R. Jin, C. Yin, M. Wang, J. Wang and S. Gao, Photoelectrocatalytic removal of dye and Cr(VI) pollutants with Ag_2S and Bi_2S_3 co-sensitized TiO_2 nanotube arrays under solar irradiation, *Sep. Purif. Technol.*, 2017, **172**, 303–309.

51 W. Fan, S. Jewell, Y. She and M. K. H. Leung, In situ deposition of Ag–Ag_2S hybrid nanoparticles onto TiO_2 nanotube arrays towards fabrication of photoelectrodes with high visible light photoelectrochemical properties, *Phys. Chem. Chem. Phys.*, 2014, **16**, 676–680.

52 J. M. Mazurków, A. Kusior, A. Mikuła and M. Radecka, Transition metal sulfides for electrochemical applications: Controlled chemical conversion of CuS to Ag_2S, *Appl. Surf. Sci.*, 2022, **606**, 154984.

53 W. Chen, H. Wang, H. Tang, C. Yang and Y. Li, Unique Voltammetry of Silver Nanoparticles: From Single Particle to Aggregates, *Anal. Chem.*, 2019, **91**, 14188–14191.

54 D. Sarkar, K. G. Chandan, S. Mukherjee and K. K. Chattopadhyay, Three Dimensional Ag_2O/TiO_2 Type-II (p–n) Nanoheterojunctions for Superior Photocatalytic Activity, *ACS Appl. Mater. Interfaces*, 2013, **5**, 331–337.

55 J. P. Allen, D. O. Scanlon and G. W. Watson, Electronic structures of silver oxides, *Phys. Rev. B: Condens. Matter Mater. Phys.*, 2011, **84**, 115141.

56 I. Martina, R. Wiesinger and M. Schreiner, Micro-Raman investigations of early stage silver corrosion products occurring in sulfur containing atmospheres, *J. Raman Spectrosc.*, 2013, **44**, 770–775.

57 S. I. Sadovnikov, E. G. Vovkotrub and A. A. Rempel, Micro-Raman Spectroscopy of Nanostructured Silver Sulfide, *Dokl. Phys. Chem.*, 2018, **480**, 81–84.

58 H. Luo, X. Jib and S. Cheng, Investigation into the electrochemical behaviour of silver in alkaline solution and the influence of Audecoration using operando Raman spectroscopy, *RSC Adv.*, 2020, **10**, 8453.

59 L. Peng, S. Shoaib, A. Shah and Z. Wei, Recent developments in metal phosphide and sulfide electrocatalysts for oxygen evolution reaction, *Chin. J. Catal.*, 2018, **39**, 1575–1593.

60 J. G. Horstmann, H. Böckmann and B. Wit, Coherent control of a surface structural phase transition, *Nature*, 2020, **583**, 232–236.

61 G. I. N. Waterhouse, G. A. Bowmaker and J. B. Metson, The thermal decomposition of silver (I, III) oxide: A combined XRD, FT-IR and Raman spectroscopic study, *Phys. Chem. Chem. Phys.*, 2001, **3**, 3838–3845.